Computational Fluid Dynamics Capability for the Solid-Fuel Ramjet Projectile

Michael J. Nusca*
U.S. Army Ballistic Research Laboratory, Aberdeen Proving Ground, Maryland
and
Sukumar R. Chakravarthy† and Uriel C. Goldberg‡
Rockwell International Science Center, Thousand Oaks, California

A computational fluid dynamics solution of the Navier-Stokes equations has been applied to the internal and external flow of inert solid-fuel ramjet projectiles. Computational modeling reveals internal flowfield details not attainable by flight or wind-tunnel measurements, thus contributing to the current investigation into the flight performance of solid-fuel ramjet projectiles. The present code employs numerical algorithms termed total variational diminishing (TVD). Computational solutions indicate the importance of several special features of the code, including the zonal grid framework, the TVD scheme, and a recently developed backflow turbulence model. The solutions are compared with results of internal surface pressure measurements. As demonstrated by these comparisons, the use of a backflow turbulence model distinguishes between satisfactory and poor flowfield predictions.

Nomenclature

C_p	= specific heat capacity at constant pressure
C_v	= specific heat capacity at constant volume
D	= diameter
e	= specific total internal energy
F,G,H	= fluxes [Eq. (1)]
k	= kinetic energy of turbulence
M	= Mach number
n	= 0.64874 [Eq. (11)]
Pr	= Prandtl number
p	= pressure
q	= heat
T	= temperature
t	= time
U	= mean streamwise velocity
u,v,w	= Cartesian velocity components
W	= dependent variable vector [Eq. (1)]
x,y	= Cartesian coordinates
α	= flow dimensionality index [Eq. (1)]
γ	= ratio of specific heats, $= C_p/C_v$
ϵ	= isotropic part of turbulence energy dissipation
η	= transformed coordinate
μ	= molecular viscosity
ξ	= transformed coordinate
ρ	= density
σ_{rr},σ_{xx}	= normal stress tensor
τ	= transformed time
τ_{xr}	= shear stress tensor

Superscript

$(\dot{})$	= rate

Subscripts

inj	= injector
nt	= nozzle throat
o	= total or stagnation value
r	= r derivative
t	= turbulence quantity
x	= x derivative
η	= η-direction transform coefficient
ξ	= ξ-direction transform coefficient
∞	= freestream quantity

Introduction

VARIOUS solid-fuel, tubular ramjet projectiles have been developed at the U.S. Army Ballistic Research Laboratory (BRL).[1,2] One of these projectiles has been designed for use as a tank gun training round (TGTR) for the 105-mm, M68 tank cannon. The goal of the program is to demonstrate a TGTR of low dispersion at 3 km and a maximum (safety) range of 8 km. The concept of the TGTR is to use the thrust (hence low drag) of the solid-fuel ramjet (SFRJ) projectile to obtain a ballistic match with low-drag kinetic energy projectiles up to 3 km. Upon depletion of the solid propellant and choking of the internal flow, the SFRJ will become a high-drag projectile with limited range. The successful demonstration of the SFRJ projectile has included the verification of flight and motor performance, limited safety range, and ballistic match to a kinetic energy projectile up to 2.5 km with somewhat higher dispersion than desired. Investigations into the combustion efficiency are currently underway in an effort to extend the ballistic match to 3 km. Computational flow modeling significantly contributes to this investigation by adding to the current understanding of the SFRJ internal flow.

A computational fluid dynamics (CFD) code utilizing an implicit, factored, time-stepping algorithm in a zonal grid framework has been developed by Chakravarthy.[3] This code employs a class of numerical algorithms, termed total variational diminishing (TVD), that do not require the inclusion of smoothing or dissipation functions to achieve numerical stability. The code can be used in conjunction with various turbulence and separated flow modeling techniques. Modeling

Received July 29, 1988; revision received Feb. 17, 1989. This paper is declared a work of the U.S. Government and is not subject to copyright protection in the United States.

*Aerospace Engineer. Member AIAA.
†Manager, Computational Fluid Dynamics Department. Member AIAA.
‡Member Technical Staff. Member AIAA.

strategies investigated include 1) the Baldwin-Lomax turbulence model[4] applied throughout the flowfield, and 2) the Baldwin-Lomax model applied outside of backflow regions, and the backflow turbulence model of Goldberg[5] applied within these regions. This code has been previously employed in the solution of subsonic, transonic, supersonic, and mixed-flow problems including complex supersonic inlet and nozzle flows by Chakravarthy et al.[6-9,11] and Sova.[10] This paper describes application of the code to an inert SFRJ projectile. Results for axisymmetric (zero yaw) cold flow (no combustion or mass injection) are presented.

Previous computational efforts include the application of an unsteady, thin-layer Navier-Stokes code to ramjet-type configurations[12] and an axisymmetric method of characteristics solution for ramjet inlet flow.[13] The latter solution assumed separated flow in the inlet and an experimentally determined inlet pressure level.

The SFRJ flight vehicle has a 43.18-mm-diam injector and a 39.12-mm-diam nozzle. During wind-tunnel tests, small changes in total pressure produced dramatically different internal wall pressure distributions that were not observed for other injector/nozzle diameter combinations.[14,15] This unusual behavior could reflect bistable flow or highly complex flow states for this configuration. Comparisons between computed and measured internal wall pressures are made for several injector/nozzle diameter combinations and a single total pressure for which stable wall static pressures were observed. The detailed analysis of the effect of different total pressures for the flight vehicle is not addressed in this paper.

Cold flow, zero-yaw computations, for which internal flow measurements exist, are a necessary prelude to further extensions of the computational analysis for the SFRJ projectile. Recently, various aerothermodynamic options (perfect gas, real gas including equilibrium and nonequilibrium chemistry) have been incorporating into the code.[16] After testing and validation, these reacting flow computations can be extended to the three-dimensional case (nonzero yaw) for direct comparisons with measured aerodynamic drag.

Computational Approach

The present CFD approach can be used to predict the compressible flowfield in and around an aerodynamic projectile by solving the three-dimensional Navier-Stokes equations. At present only axisymmetric (zero-yaw) flows have been investigated. These equations are solved with the assumption that the flow medium is air behaving as a perfect gas and that no chemical reactions are occurring. As a result, only inert SFRJ projectiles are addressed at present. Both laminar and turbulent flows are investigated. Thus, an adequate turbulence model is required for closure. The internal geometry incorporates several forward- and backward-facing steps. Therefore, backflow regions can be present; thus, a backflow turbulence model is included. The equations are transformed into conservation law form and discretized using finite-volume approximations and the TVD formulation. The resulting set of equations is solved using an implicit, factored, time-stepping algorithm. This solution takes place on a computational grid that is generated around the projectile in zones where the zonal boundaries can be made transparent to the flowfield calculation.

Equations of Motion

The compressible, Reynolds-averaged Navier-Stokes equations for two-dimensional/axisymmetric flow are written in the following conservation form (the dependent variables u, v, and e are mass-averaged):

$$\frac{\partial W}{\partial t}+\frac{\partial F}{\partial x}+\frac{\partial G}{\partial y}+\left(\frac{G}{y}-\frac{H}{y}\right)\alpha=0 \tag{1a}$$

$$W=\begin{bmatrix}\rho\\ \rho u\\ \rho v\\ \rho e\end{bmatrix},\quad F=\begin{bmatrix}\rho u\\ \rho u^2-\sigma_{xx}\\ \rho uv-\tau_{xr}\\ \rho ue+\dot{q}_x-\sigma_{xx}u-\tau_{xr}v\end{bmatrix}$$

$$G=\begin{bmatrix}\rho v\\ \rho uv-\tau_{xr}\\ \rho v^2-\sigma_{rr}\\ \rho ve+\dot{q}_r-\tau_{xr}u-\sigma_{rr}v\end{bmatrix} \tag{1b}$$

$$H=\begin{bmatrix}0\\ 0\\ -\sigma_+\\ 0\end{bmatrix} \tag{1c}$$

$$\sigma_{xx}=-p-\frac{2}{3}(\mu+\mu_t)\nabla\cdot U+2(\mu+\mu_t)\frac{\partial u}{\partial x} \tag{2}$$

$$\sigma_{rr}=-p-\frac{2}{3}(\mu+\mu_t)\nabla\cdot U+2(\mu+\mu_t)\frac{\partial v}{\partial y} \tag{3}$$

$$\sigma_+=-p-\frac{2}{3}(\mu+\mu_t)\nabla\cdot U+2(\mu+\mu_t)\frac{v}{y}\alpha \tag{4}$$

$$\tau_{rx}=\tau_{xr}=(\mu+\mu_t)\left(\frac{\partial u}{\partial y}+\frac{\partial v}{\partial x}\right) \tag{5}$$

$$\dot{q}_x=-C_p\left(\frac{\mu}{Pr}+\frac{\mu_t}{Pr_t}\right)\frac{\partial T}{\partial x} \tag{6}$$

$$\dot{q}_r=-C_p\left(\frac{\mu}{Pr}+\frac{\mu_t}{Pr_t}\right)\frac{\partial T}{\partial y} \tag{7}$$

$$e=C_vT+\tfrac{1}{2}(u^2+v^2) \tag{8}$$

$$\nabla\cdot U=\frac{\partial u}{\partial x}+\frac{\partial v}{\partial y}+\frac{v}{y}\alpha \tag{9}$$

where $\alpha=1$ for axisymmetric flow and 0 for two-dimensional flow.

In Eqs. (2-7), the laminar and eddy viscosities μ and μ_t are implicitly divided by the reference Reynolds number. The equations used for the Euler (inviscid) calculations are obtained from Eqs. (1-9) by setting both laminar and eddy viscosities to zero. In all calculations, the flow medium (air) was assumed to be a perfect gas, satisfying the equation of state

$$p=\rho RT \tag{10}$$

The following power law was used to relate molecular viscosity to temperature[17]:

$$\frac{\mu}{\mu_o}=\left(\frac{T}{T_o}\right)^n \tag{11}$$

where $\mu_o=0.1716$ mP, $T_o=491.6°R$, and $n=0.64874$. The laminar and turbulent Prandtl numbers Pr and Pr_t were assumed constant with values of 0.72, and 0.9, respectively. The γ was also assumed constant and equal to 1.4.

Assuming a time-invariant grid, under the transformation of coordinates implied by $\tau=t$, $\xi=\xi(x,y)$, and $\eta=\eta(x,y)$,

Eqs. (1) can be recast into the conservation form given by[6]

$$\frac{\partial W}{\partial \tau} + \frac{1}{\text{area}}\left[(y_\eta F - x_\eta G)_\xi + (-y_\xi F + x_\xi G)_\eta + \frac{G}{y} - \frac{H}{y}\right] = 0 \tag{12}$$

where ξ and η are the new independent variables and x_ξ, x_η, y_ξ, and y_η are the four transformation coefficients obtained numerically from the mapping procedure. The "area" in Eq. (12) denotes the area of the finite-volume cell under consideration at the time of discretization of the equations.

Turbulence Modeling

The internal flowfield of the SFRJ projectile can include large regions of recirculating flow, induced by both shock waves and sharp geometric discontinuities. Indeed, internal surface pressure measurements made on an instrumented SFRJ wind-tunnel model (unfueled) indicate that such regions do exist in the inlet and combustion sections.[14,15] Good modeling of these regions is critical to the overall flowfield solution quality. However, most existing turbulence models either do not treat such regions or do so in a semiempirical fashion that is frequently inadequate. A notably different approach is the use of a Reynolds stress closure model, involving the solution of five coupled partial differential equations (for two-dimensional flows) for three normal stresses, the shear stress, and the length scale. These must be supplemented by a wall function to provide turbulence quantities across viscous regions adjacent to solid surfaces. Such a wall function is usually some form of the law of the wall, which, according to experimental observations, does not apply to detached flows. Thus, an expensive and time-consuming computation of the Reynolds stresses is coupled with a questionable near-wall formulation.

To improve the predictive capability of separated flows using current Reynolds-averaged Navier-Stokes codes, a new turbulence model has been recently developed.[5] The new turbulence model is based on experimental observations of detached flows. The model prescribes k and ϵ analytically within backflows. A Gaussian variation of k normal to walls is assumed. The length scale of turbulence is proportional to the local distance from the wall to the edge of the viscous sublayer, which is located outside the backflow region. The latter feature is a basic assumption of the model. The stress scale is the local maximum Reynolds stress, which typically occurs around the middle of the boundary layer, well outside the separation bubble. This scale must be supplied by a turbulence model that is used beyond backflow regions.

The main equations of the backflow model are given in Ref. 5. A formula for the eddy viscosity distribution within backflows is derived and used to supply eddy viscosity for the Reynolds-averaged equations when the calculations are done inside separation bubbles. Outside of them, another turbulence model (e.g., Baldwin-Lomax[4]) supplies the values of eddy viscosity. Whereas the Baldwin-Lomax turbulence model is used to detect flow separation and to initiate application of the backflow model, the latter model can relocate the separation point (and the reattachment point, if one exists). The location of flow separation as predicted by the Baldwin-Lomax turbulence model and Goldberg's backflow model are significantly different for the applications reported in Ref. 18. For further details of how the model treats the influence of large eddies residing outside the detached regions, the history effect of these eddies downstream of reattachement, and the mutual influence of multiple walls on the eddy viscosity (see Ref. 18). The model has been tested successfully for a variety of flow conditions and body geometries, including a backward-facing step in subsonic flow,[18] an axisymmetric bump in transonic flow,[18] and an axisymmetric boattail in transonic flow.[19]

Computational Algorithm

The spatial discretization technique for the equations of motion must be reliable and robust if it is to capture successfully the complex physics of SFRJ internal and external flowfields. The TVD formulation for the convective terms (the hyperbolic part of the time-dependent Navier-Stokes equations), along with a special treatment of the dissipative terms, provide an appropriate simulation. Any conventional time discretization method, suitable for the Navier-Stokes equations, (e.g., approximate factorization and relaxation techniques) can be used together with the space discretization methodology described earlier. In recent years, TVD formulations have been constructed for shock-capturing finite-difference methods.[6-9] Near large gradients in the solution (extrema), TVD schemes automatically reduce to first-order-accurate discretizations locally, whereas away from extrema they can be constructed to be of higher-order accuracy. This local effect restricts the maximum global accuracy possible for TVD schemes to third order for steady-state solutions.

These methods manifest many properties desirable in numerical solution procedures. By design, they avoid numerical oscillations and "expansions shocks" while at the same time being higher-order (more than first-order) accurate. (Expansion shocks are shock waves that do not satisfy the entropy inequality.) TVD formulations are also based on the principle of discrete or numerical conservation, which is the numerical analog of physical conservation of mass, momentum, and energy. As a result, TVD schemes can "capture" discontinuities with ease and high resolution. At a fundamental level, they are based on upwind schemes; therefore, they closely simulate the signal propagation properties of hyperbolic equations.

Schemes based on the TVD formulation are completely defined. In other words, the user does not have to specify any "numerical coefficients" to be able to carry out the computations. In contrast, central-difference schemes involve dissipation terms for stability and have one or more coefficients that must be judiciously chosen to achieve desirable results. Methods based on TVD formulations represent mature CFD technology and are being applied to a wide class of problems.[8]

Proper treatment of the dissipative terms of the Navier-Schemes equations is also important in the construction of reliable numerical methods. Unidirectional second derivative terms are treated by using central-difference approximations. Cross derivatives are represented by finite-differences, the nature of which depends on the sign of the coefficient of such terms. This treatment augments diagonal dominance of the resulting set of discretized equations without detracting from the accuracy and while adding to the reliability of the numerical procedure. Further details can be found in Ref. 6. The diagonal dominance of TVD schemes (with suitable discretized cross-derivative terms) makes it possible to use relaxation methods. However, conventional approximate factorization methods are used to solve multidimensional implicit formulations in the present study.

Computational Grid

The problem of computing internal/external SFRJ projectile flowfields is complicated by the internal geometry involved. As illustrated in Fig. 1, the SFRJ consists of several sharp corners that would severely hamper conventional grid generation schemes that require one set of grid lines to be tangent to the surface and another set to be normal to it.[12] The SFRJ geometry is more easily gridded by the zonal approach. The internal geometry of the SFRJ in broken up into four zones of simple geometric shape (Fig. 2). In each zone any approach to generating the grid can be used, such as algebraic methods, differential equation methods, etc. In this case a simple algebraic grid is used with grid clustering near the surface and other regions where high gradients are expected (Fig. 3). In the zonal approach, the computational method and computer program are constructed in such a manner that

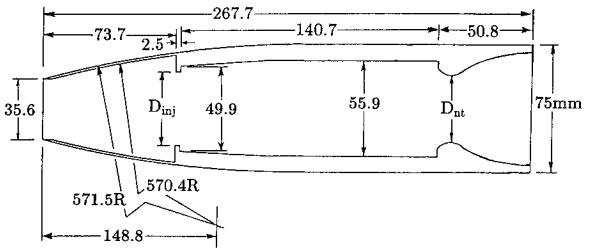

Fig. 1 SFRJ geometry; $D_{inj} = 43.18$, 48.26 mm; $D_{nt} = 27.94$, 39.12, 40.64 mm.

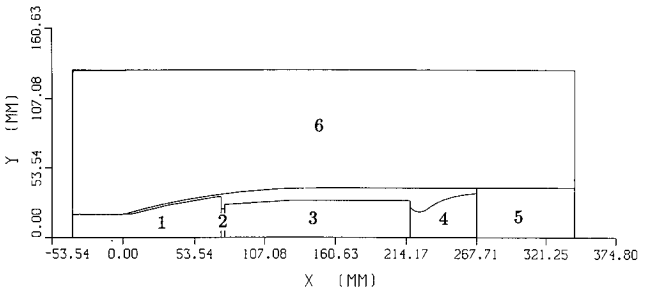

Fig. 2 Zone designations for axisymmetric SFRJ geometry; 1: inlet, 2: injector, 3: combustion section, 4: nozzle, 5: base, 6: exterior.

each zone may be considered as an independent module, interacting with the others before or after the information corresponding to each zone is updated one cycle. In addition, the zonal boundaries can be made transparent to flowfield phenomena (e.g., shock waves). The actual grid used for these computations consisted of the following dimensions for zones 1-6: 60×61, 7×30, 80×49, 40×30, 15×49, and 45×20. These grid dimensions represent a refinement over a coarse grid that was initially used (30×35, 7×17, 50×30, 30×17, 15×25, 45×20).[3] The computational results were found to be essentially independent of these two grids when all other factors (e.g., flow turbulence and transition modeling) were the same. However, the fine grid was preferred for resolving flow details within boundary layers. The grids have been generated in such a manner that the horizontal families of mesh lines within the projectile are continuous between zones and the vertical families are continuous in the zones external to the SFRJ. Although this type of grid is natural for this problem, the computational methodology permits a wider class of patched zonal grids where neither family of grid lines needs to be continuous across zones.

Results

The computational solutions are compared with internal surface pressure measurements of an inert SFRJ. The model was instrumented with pressure taps and mounted in the Mach 4, 9-in. blowdown tunnel at the NASA Langely Research Center. The details of these test are described in Ref. 14. The freestream Mach number and Reynolds number were 4.03 and about 66 million per meter, respectively. The model was at zero yaw.

In the computational solutions, the freestream Mach number was increased gradually as the numerical iterations progressed. At a given point in the iteration cycle, the Mach number was fixed and the iterations continued until convergence. For the Euler (inviscid) solutions, the Mach number was linearly increased from 0.03 to 4.03 for 3000 iterations and then held fixed for the balance of 5000 total iterations. For the Navier-Stokes solutions, the Mach number was linearly increased from 0.03 to 4.03 for 1000 iterations and then held fixed for the balance of 5000 total iterations. The more

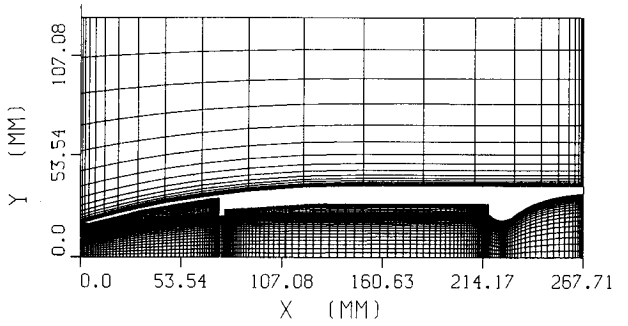

Fig. 3 Computational grid for axisymmetric SFRJ (near field shown).

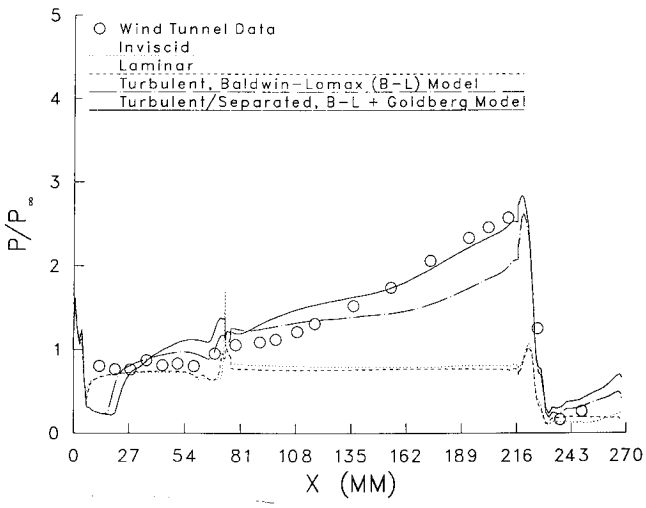

Fig. 4 Internal surface presure distribution for SFRJ; $M_\infty = 4.03$, 43.18-mm-diam injector, 40.64-mm-diam nozzle. Effect of viscous modeling.

conservative treatment for the Euler cases was necessary given the complex geometry of the SFRJ and the lack of natural viscosity to damp transients developing in the inviscid flow. In all cases convergence was determined by the arrival at a time-asymptotic steady-state solution. The Courant-Friedrichs-Levy (CFL) number for these results was set at 1.0 for the Euler solutions, and between 0.5 and 2.5 for the Navier-Stokes solutions, although solutions can be achieved in about 1000 iterations with CFL numbers as high as 10. Typical run times on a Cray X-MP/48 computer for Euler and Navier-Stokes solutions were 0.8 and 1.2 CPU h, respectively.

The Navier-Stokes solutions consisted of both laminar and turbulent cases. In the turbulent cases the Baldwin-Lomax model was used both with and without the Goldberg backflow model previously described. The latter model was invoked only if the computed flow conditions (based on the Baldwin-Lomax model) indicated flow separation. If this condition did not occur, the Baldwin-Lomax model was used exclusively. Because of the zonal nature of the code, a flow type (laminar or turbulent) can be assigned to each zone, or all zones can be solved with the same flow type assumption.

Importance of Flow Turbulence and Transition

Figure 4 shows computed internal wall pressure distributions for the configuration with a 43.18-mm-diam injector and a 40.64-mm-diam nozzle. The code was run assuming inviscid, laminar, turbulent, and turbulent/detached flow. For the turbulent cases, transition from laminar to turbulent flow was specified near the leading edge of the inlet. The best overall agreement of the computations with pressure data in the com-

bustion section ($75 \leq x \leq 230$ mm) is achieved when the backflow turbulence model is used. In this section, the flow can be characterized as turbulent and detached. Studies of the computed flow velocity vectors indicate that the combustion region is dominated by a separation bubble. Here, the flow separation point is determined by the sharp corner of the injector.

In the inlet ($0 \leq x < 75$ mm) the computations with turbulence predict an expansion at the leading edge, followed by a gradual compression that starts at about one-third the inlet length from the leading edge (i.e., the flow separation point). The Baldwin-Lomax turbulence model predicts the separation point slightly further forward than the backflow turbulence model of Goldberg. However, the wind-tunnel data show a constant pressure over the entire inlet, indicating flow separation at or near the leading edge of the inlet. Unexpectedly, the computations assuming laminar flow better match the data in the inlet. This result suggests that either 1) the inlet flow is turbulent and detached but the Baldwin-Lomax turbulence model and the Goldberg backflow model predict flow separation further rearward than indicated by the wind-tunnel data, or 2) the inlet flow is transitional (i.e., neither fully turbulent nor laminar) and the point of transition from laminar to turbulent flow cannot be arbitrarily specified.

Figure 5 shows the effects of flow transition location on turbulent/detached flow computations for the configuration with a 43.18-mm-diam injector and a 40.64-mm-diam nozzle. For the two computations shown, flow transition has been specified at either the beginning of the inlet or at the end of the inlet (i.e., at the injector). For the latter case, the inlet flow is computed as laminar, and the best overall comparison with wind-tunnel data, in this region, is achieved. Studies of the computed flow velocity vectors indicate that a large separation bubble extends over the entire inlet length. The laminar flow assumption more accurately predicts the separation point in the inlet. This result is unexpected since laminar/separated flows are unusual. However, as stated earlier, the turbulence models employed may be deficient in predicting the flow separation point in the inlet. Specifying transition at the injector improves agreement with data behind the injector but degrades agreement at the end of the combustion section. For the entire configuration, the best overall agreement between computed and measured wall pressures is achieved for injector transition.

Figure 6 shows the results of a similar flow transition study for a configuration with a 48.26-mm-diam injector and a 27.94-mm-diam nozzle. In contrast to the 40.64-mm-diam nozzle, the smaller nozzle diameter causes a normal shock at the leading edge of the SFRJ with subsonic flow throughout the interior. For this configuration, the best overall agreement with wind-tunnel data occurs when flow transition is specified at the beginning of the inlet. In this case, the normal shock has determined the point of flow separation.

In summary, the SFRJ configurations studied to date indicate that flow transition may occur at the beginning of the inlet for subsonic cases (nozzle diameter 27.94 mm) and at the end of the inlet for supersonic cases (nozzle diameter 40.64 mm). This criterion was used to locate flow transition for all subsequent computations.

Discussion of Computed Results

Figure 7 shows comparisons of internal surface pressure measurements and turbulent/detached flow computations for three SFRJ configurations. The configuration used in SFRJ flight tests (43.18-mm-diam injector and 39.12-mm-diam nozzle) is included. These configurations differ only in the nozzle diameter (40.64, 39.12, or 27.94 mm). The injector diameter was 43.18 mm for each case. The criterion established in the preceding section was used to specify the flow transition location. The lower pressure level for the 40.64-mm and 39.12-mm-diam nozzle configurations is indicative of supersonic internal flow, with the exception of the wall boundary layers and detached regions. The overall agreement between computation and measurements is notably better than that for the 27.94-mm-diam nozzle.

The higher pressure level for the 27.94-mm-diam nozzle indicates subsonic internal flow caused by an expelled leading-edge normal shock. The computed wall pressure matches the distribution but not the level of the measured pressure. Indeed, the computed pressure level better matches the measured result for the 30.48-mm-diam nozzle (see Fig. 10 of Ref. 3). This result indicates a nozzle wall boundary-layer thickness that is predicted to be thinner that the actual one. This discrepancy could be caused by a turbulence model deficiency, since these computed pressures were found to be independent of grid resolution normal to the nozzle wall. Investigations with other turbulence models should clarify this point.

Figure 8 shows the pressure contours for the 40.64-mm-diam nozzle SFRJ. An oblique shock is attached to the leading edge of SFRJ and intersects the centerline of the model as a normal shock. Examination of the computed velocity vectors shows that the inlet flow is dominated by a separation bubble

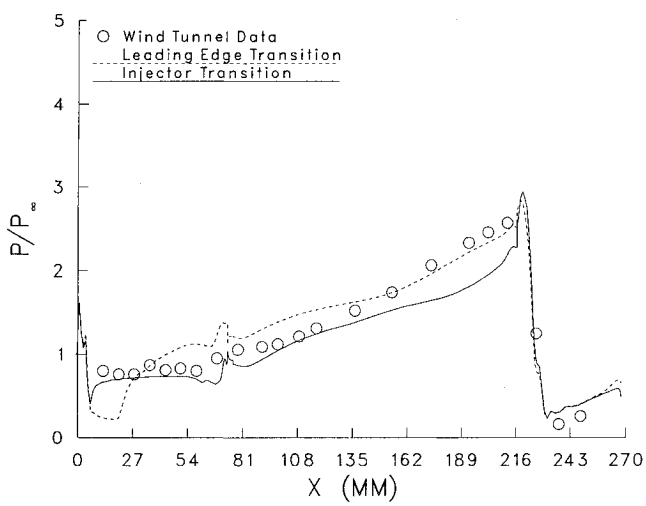

Fig. 5 Internal surface pressure distribution for SFRJ; $M_\infty = 4.03$, 43.18-mm-diam injector, 40.64-mm-diam nozzle. Effect of flow transition location.

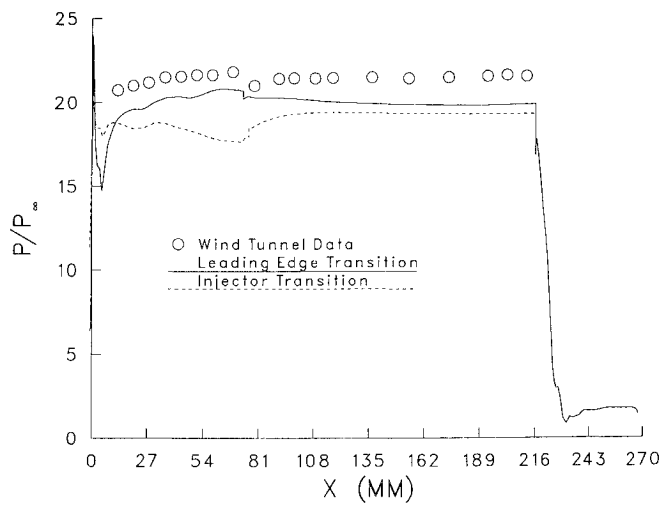

Fig. 6 Internal surface pressure distribution for SFRJ; $M_\infty = 4.03$, 48.26-mm-diam injector, 27.94-mm-diam nozzle. Effect of flow transition location.

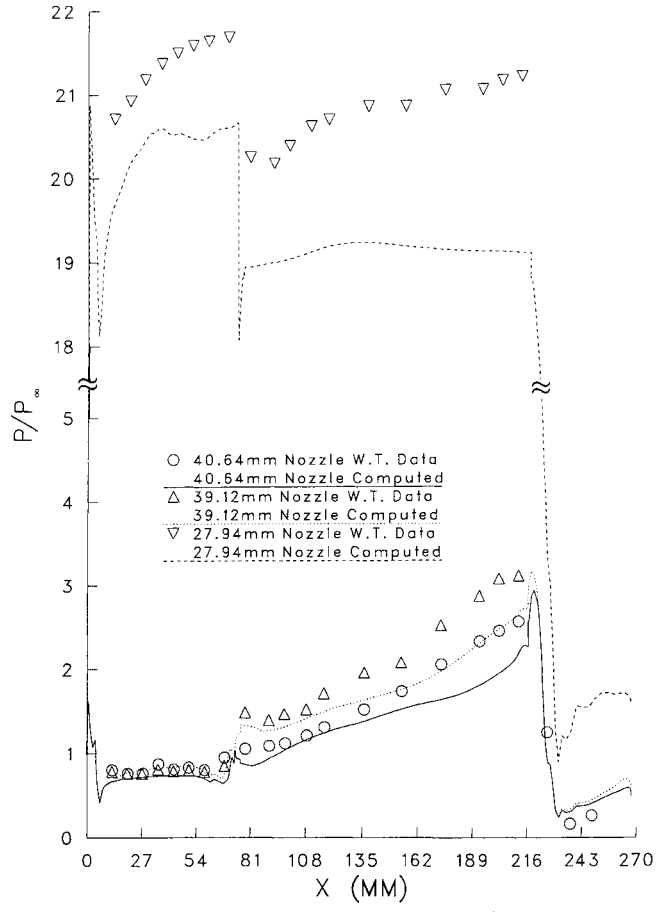

Fig. 7 Internal surface pressure distribution for SFRJ; $M_\infty = 4.03$, 43.18-mm-diam injector, 27.94-, 39.12-, and 40.64-mm-diam nozzles.

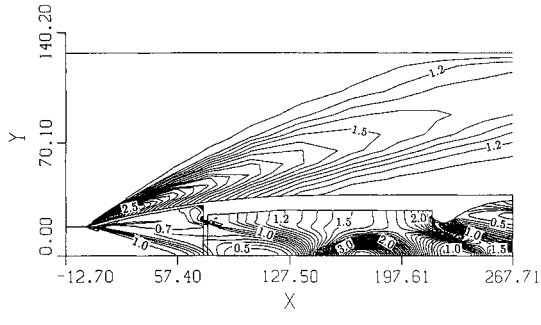

Fig. 8 Pressure contours for SFRJ; $M_\infty = 4.03$, 43.18-mm-diam injector, 40.64-mm-diam nozzle.

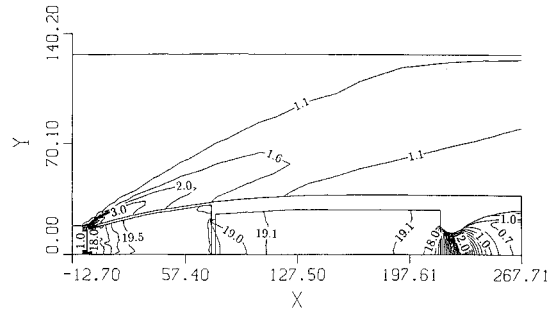

Fig. 9 Pressure contours for SFRJ; $M_\infty = 4.03$, 43.18-mm-diam injector, 27.94-mm-diam nozzle.

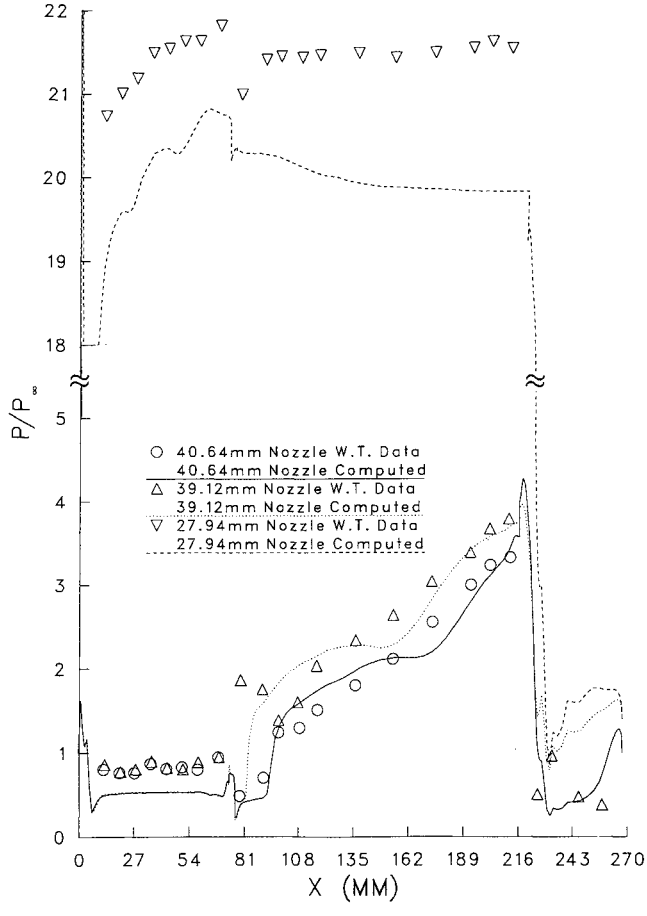

Fig. 10 Internal surface pressure distribution for SFRJ; $M_\infty = 4.03$, 48.26-mm-diam injector, 27.94-, 39.12-, and 40.64-mm-diam nozzles.

that terminates at the injector where an oblique shock is generated. The flow in the combustion section is also dominated by a separation bubble that extends from the injector to the nozzle and well into the flowfield. A zero wall pressure gradient extends throughout this region (see Fig. 8). Several shock reflections occur throughout the combustion and nozzle sections.

Figure 9 shows the pressure contours for the 27.94-mm-diam nozzle SFRJ. A normal shock is clearly seen at the leading edge. Upon detailed examination, the presence of flow spillage to the exterior has been found. The subsonic interior flow expands through the diverging inlet, and the pressure remains relatively constant throughout the combustion section. Expansion back to supersonic flow is accomplished by the nozzle. Examination of the computed velocity vectors shows that the inlet flow separates at about two-thirds of the length from the leading edge. In the combustion section a large separation bubble is established behind the injector that thins to a narrow region of separated flow near the wall of the combustor. In contrast, a larger nozzle diameter (40.64 mm) produces large separated flow regions that dominate both the inlet and the combustion sections.

Figure 10 shows comparisons between internal surface pressure measurements and turbulent/detached flow computations for three SFRJ configurations with an injector diameter of 48.26 mm and nozzle diameters of 40.64, 39.12, and 27.94 mm. The criterion established in the preceding section was used to specify the flow transition location. The similarity of

these results with those for the 43.18-mm-diam injector (Fig. 7) indicates the relative insignificance of the injector diameter in determining the internal wall pressures.

Conclusions

Computational solutions of the internal and external flowfield for inert SFRJ projectiles at zero yaw have been performed using a zonal Navier-Stokes code with a TVD scheme. Comparisons between computed and measured internal surface pressures were made.

The flow transition location was guided by measured internal wall pressure data and was chosen to achieve the best overall agreement with measured data. Although the inlet flow transition point is determined by the expelled normal shock for subsonic internal flow (27.94-mm nozzle diameter), for supersonic flow (40.64-mm-diam nozzle), the transition point location is unclear. The best agreement with measured wall pressures is achieved when flow transition is specified at the end of the inlet (at the injector). The best overall agreement with the measured pressure level and gradient along the combustion section was achieved using the backflow turbulence model of Goldberg.

The agreement with measured internal wall pressures ensures that computed flow predictions can correctly replicate physical flow details. This agreement was achieved with the aid of experimental data to guide the location of flow transition. These computations indicate that nozzle diameters of about 40.64 mm yield a leading-edge oblique shock and supersonic core flow. The inlet and combustion sections are dominated by flow detachment. A nozzle diameter of 27.94 mm yields an expelled leading-edge normal shock, subsonic internal flow, and a choked nozzle.

References

[1]Mermagen, W. H., and Yalamanchili, R. J., "First Diagnostic Tests of a 75 mm Solid Fuel Ramjet Tubular Projectile," U.S. Army Ballistic Research Laboratory, Aberdeen Proving Ground, MD, ARBRL-03283, June 1983.

[2]Mermagen, W. H., and Yalamanchili, R. J., "Experimental Tests of a 105/75 mm Solid Fuel Ramjet Tubular Projectile," U.S. Army Ballistic Research Laboratory, Aberdeen Proving Ground, MD, ARBRL-MR-3416, Dec. 1984.

[3]Chakravarthy, S. R., "A New Computational Capability for Ramjet Projectiles," U.S. Army Ballistic Research Laboratory, Aberdeen Proving Ground, MD, ARBRL-CR-595, March 1988; see also Goldberg, U., Chakravarthy, S., and Nusca, M., "A New Computational Capability for Ramjet Projectiles," AIAA Paper 87-2411, Aug. 1987.

[4]Baldwin, B. S., and Lomax, H., "Thin Layer Approximation and Algebraic Model for Separated Turbulent Flows," AIAA Paper 78-257, Jan. 1978.

[5]Goldberg, U. C., "Separated Flow Treatment with a New Turbulence Model," *AIAA Journal*, Vol. 24, No. 10, Oct. 1986, pp. 1711–1713.

[6]Chakravarthy, S. R., and Szema, K. Y., Goldberg, U. C., Gorski, J. J., and Osher, S., "Application of a New Class of High Accuracy TVD Schemes to the Navier-Stokes Equations," AIAA Paper 85-0165, Jan. 1985.

[7]Chakravarthy, S., and Szema, K., "An Euler Solver for Three-Dimensional Supersonic Flows with Subsonic Pockets," AIAA Paper 85-1703, July 1985.

[8]Chakravarthy, S. R., "The Versatility and Reliability of Euler Solvers Based on High-Accuracy TVD Formulations," AIAA Paper 86-0243, Jan. 1986.

[9]Chakravarthy, S. R., Harten, A., and Osher, S., "Essentially Non-Oscillatory Shock-Capturing Schemes of Arbitrarily-High Accuracy," AIAA Paper 86-0339, Jan. 1986.

[10]Sova, G. J., "Application of Navier-Stokes Analysis to Predict the Internal Performance of Thrust Vectoring Two-Dimensional Convergent-Divergent Nozzles," AIAA Paper 88-2586, June 1988.

[11]Chakravarthy, S. R., Szema, K., and Haney, J. W., "Unified Nose-to-Tail Computational Method for Hypersonic Vehicle Applications," AIAA Paper 88-2564, June 1988.

[12]Nietubicz, C. J., and Heavey, K. R., "Computational Flow Field Predictions for Ramjet and Tubular Projectiles," *Proceedings of the 8th International Symposium on Ballistics*, American Defense Preparedness Association, Arlington, VA, 1984, pp. FD17-FD26.

[13]Danberg, J. E., and Sigal, A., "Evaluation of Solid Fuel Ramjet Projectile Aerodynamic Characteristics," *Proceedings of the 10th International Symposium on Ballistics*, American Defense Preparedness Association, 1987, pp. FD67-FD76.

[14]Kayser, L. D., Yalamanchili, R. J., and Trexler, C., "Pressure Measurements on the Interior Surface of a 75 mm Tubular Projectile at Mach 4," U.S. Army Ballistic Research Laboratory, Aberdeen Proving Ground, MD, ARBRL-MR-3725, Dec. 1988.

[15]Davis, B., and Yalamanchili, R. J., unpublished wind tunnel data for a 75-mm tubular projectile at Mach 4, U.S. Army Ballistic Research Laboratory, Aberdeen Proving Ground, MD, 1988.

[16]Palaniswamy, S., and Chakravarthy, S. R., "Finite Rate Chemistry for USA-Series Codes: Formulation and Applications," AIAA Paper 89-0200, Jan. 1989.

[17]Mazor, G., Ben-Dor, G., and Igra, O., "A Simple and Accurate Expression for the Viscosity of Nonpolar Diatomic Gases up to 10,000 K," *AIAA Journal*, Vol. 23, No. 4, April 1985, pp. 636–638.

[18]Goldberg, U. C., and Chakravarthy, S. R., "Prediction of Separated Flows with a New Backflow Turbulence Model," *AIAA Journal*, Vol. 26, No. 4, April 1988, pp. 405–408.

[19]Goldberg, U. C., "Separated Flow Calculations With A New Turbulence Model," *Proceedings of the First World Congress on Computational Mechanics*, Univ. of Texas, Austin, TX, Sept. 1986.